Citation for published version:
Zheng, L, Yang, Y, Bowen, CR, Jiang, L, Shu, Z, He, Y, Yang, H, Xie, Z, Lu, T, Hu, F & Yang, W 2023, 'A high-performance UV photodetector with superior responsivity enabled by a synergistic photo/thermal enhancement of localized surface plasmon resonance', *Journal of Materials Chemistry C*, vol. 11, no. 18, pp. 6227-6238. https://doi.org/10.1039/d3tc00446e

DOI:
10.1039/d3tc00446e

Publication date:
2023

Document Version
Peer reviewed version

Link to publication

University of Bath

Alternative formats
If you require this document in an alternative format, please contact:
openaccess@bath.ac.uk

General rights
Copyright and moral rights for the publications made accessible in the public portal are retained by the authors and/or other copyright owners and it is a condition of accessing publications that users recognise and abide by the legal requirements associated with these rights.

Take down policy
If you believe that this document breaches copyright please contact us providing details, and we will remove access to the work immediately and investigate your claim.

Download date: 08. May. 2024

PAPER

High-performance UV Photodetector with Superior Responsivity Enabled by a Synergistic Photo/Thermal Enhancement of Localized Surface Plasmon Resonance

Received 00th January 20xx,
Accepted 00th January 20xx

DOI: 10.1039/x0xx00000x

Luxia Zheng[a], Yang Yang*[a], Chris R. Bowen[b], Lan Jiang[a], Zhan Shu[a], Yun He[a], Hongli Yang[a], Zongzhuo Xie[a], Taixu Lu[a], Feng Hu *[a] and Weiyou Yang[a]

In this paper, we propose a new strategy to enhance the photoelectric performance of ultraviolet (UV) photodetectors by exploiting a synergistic photo-thermal effect which is induced by a localized surface plasmon resonance. We demonstrate that a $W_{18}O_{49}$ plasmonic semiconductor is able to improve the performance of target photodetectors as a result of a localized surface plasmon resonance, which increases light absorption, enhances the photothermal effect to deliver an increased photocurrent, and provides photo-induced "hot electrons" to limit carrier depletion over prolonged light illumination. Consequently, a UV photodetector based on $W_{18}O_{49}/TiO_2$ nanofibers is shown to exhibit an excellent photodetection performance with a high responsivity of up to 1.6×10^4 A/W, which is five times greater than the pure TiO_2 analogue and greatly exceeds the TiO_2-based photodetectors reported to date.

Introduction

Excessive irradiation from ultraviolet (UV) light of high energy and strong penetrating power can intensify corneal damage, thereby leading to snow blindness, retinopathy degeneration, and maculopathy [1-3]. The formulation of a rational strategy to meet the high requirements for functionalization, differentiation, and rapid response of UV light detection is therefore a matter of utmost urgency [4-6]. In the quest for innovations in photoelectric detection technologies, a variety of metal oxide semiconductor materials with a wide band-gap have been considered as candidates in ultraviolet communication [7], environmental sensing [8], flame detection [9], chemical and biological sensing [10, 11]. Among them, titania (TiO_2) has attracted significant attention due to its unique superiority with regard to chemical and thermal stability, high temperature resistance, and excellent photoelectric properties [12]. The wide-ranging applications of TiO_2 nanostructures have led to researchers realizing the significance of improving the optoelectronic performance of UV photodetectors.

To date, nanostructured semiconductors offer the possibility of achieving a high photoelectric performance, in particular by the creation of one-dimensional (1D) structures due to their remarkable properties such as highly-crystalline nature [13], high surface area [14], carrier confinement [15], and low carrier transit time[16]. However, the underlying methods to create nanostructured UV photodetectors with superior performance for application in air remain a challenge. In the last decade, research in this area has focused on the construction of heterostructure detectors, which are able to absorb and detect the photon energy and change the electron state within a heterojunction, thereby producing a built-in electric field to achieve efficient separation/transport of photoinduced carriers [17, 18]. Using this procedure, an improved photoelectric current can be obtained; however, the finite photon energy within the heterojunction has a direct affect on the amount of state change in the internal electron. As a classic plasmonic "optical antenna", noble metal nanostructures with a localized surface plasmon resonance (LSPR) possess the unique capability to concentrate and amplify the incident light intensity [19, 20]. Noble metals are frequently introduced into heterostructure detectors to improve system performance by enhancing light absorption and carrier transfer at the interface based on the plasmonic energy transfer from the noble metal to the semiconductor [21, 22]. However, a complex multi-step operation need to be adopted to obtain anisotropic-nanostructured noble metals, and the high-cost of noble metals restrict their large-scale practical application. Recently, heavily doped semiconductors such as $Cu_{2-x}S$, $Cu_{2-x}Se$, B-/P-doped Si, WO_{3-x}, and MoO_{3-x} have been widely employed as plasmonic nanostructures, which provide an economical and viable alternative to conventional noble metals. The LSPR phenomenon of these semiconductor materials originates from the collective oscillations of excess free carriers associated with ion doping or lattice vacancies, resulting in the emergence of a localized electric field near the surface of the nanostructures. The plasmonic "hot-electrons" generated by means of the resonant energy decay possess higher energies than those produced by direct light irradiation [23, 24].

In addition to photon detectors that directly absorb incident light energy, thermal detectors are also a common form of photodetector, which convert the absorbed light into thermal energy due to the motion of the crystal lattice. At present, a number of studies on semiconductor photodetectors that

[a] Institute of Micro/Nano Materials and Devices, Ningbo University of Technology, Ningbo 315211, P. R. China.
[b] Department of Mechanical Engineering, University of Bath, BA2 7AK, UK.
† Electronic supplementary information (ESI) available: Technical information and synthetic procedures.

integrating photon-conversion with thermal-conversion have been recently reported to improve the overall photo-response and meet the functional and performance requirements of new applications [25, 26]. However, the manufacture of these specific photodetectors requires a highly complex preparation technology. With the excavation of potential energy relaxation processes within plasmonic nanostructures, the intriguing possibility of developing a simple approach to achieve synergistic photo/thermal improvement of photoelectric properties is an area of high interest. Unlike conventional heating via an external supply, the LSPR-induced thermal effect provides an intriguing route to rapidly increase the temperature near the nanostructured surface [27]. On irradiation, the energy accumulated at the plasmonic surface decays in a non-radiative pathway, which generates localized high temperatures as a result of the electron kinetic energy, which can then be transferred to the metal lattice phonons.

In this study, we examine the synergistic photo/thermal effects that arise from plasmonic creating $W_{18}O_{49}$ nanostructures, which are able to enhance the optoelectronic performance of photodetectors. We report on a novel plasmonic photodetector design based on hydrothermal growth of plasmonic $W_{18}O_{49}$ onto TiO_2 via a two-step route. Our experimental results and 3D finite element modelling (FEM) simulations demonstrate that a single $W_{18}O_{49}/TiO_2$ heterojunction photodetector can exhibit significantly improved optoelectronic performance compared to pure TiO_2 photodetectors, and the LSPR-induced photothermal effect provides sufficient stability to allow it to be employed at low temperature conditions. The work therefore provides new insights in exploiting localized surface plasmon resonance (LSPR) to produce high performance photodetectors, with potential applications in future optoelectronic devices.

Results and discussion

The $W_{18}O_{49}/TiO_2$ heterostructure was fabricated through a facile two-step route, see Figure 1A. Firstly, TiO_2 nanofibers (NFs) were fabricated by an electrospinning method, which are annealed as a growth main trunk [28]. Secondly, a $W_{18}O_{49}$ hierarchical structure was grown on the surface of TiO_2 nanofiber trunks via a solvothermal reaction. The one-dimensional nanofibers produced were used to facilitate electron transport throughout the optoelectronic system. To illustrate the constitution of trunk-branched heterostructure, the morphology and microstructure of the compounds and corresponding single-component are examined via scanning electron microscopy (SEM) images in Figure 1B-D. As can be seen in Figure 1B, the synthesized TiO_2 NFs exhibit a smooth surface with an average diameter of 300 ~ 500 nm and a length of several micrometers. The solvothermal growth of $W_{18}O_{49}$ exhibits a 'sea urchin-like' appearance with unequal length nanowires with an average diameter of approximately 1.6 μm, as shown in Figure 1C. It can be observed that using a higher hydrothermal temperature results in thicker $W_{18}O_{49}$ nanowires (NWs), and selection of a suitable reaction temperature to

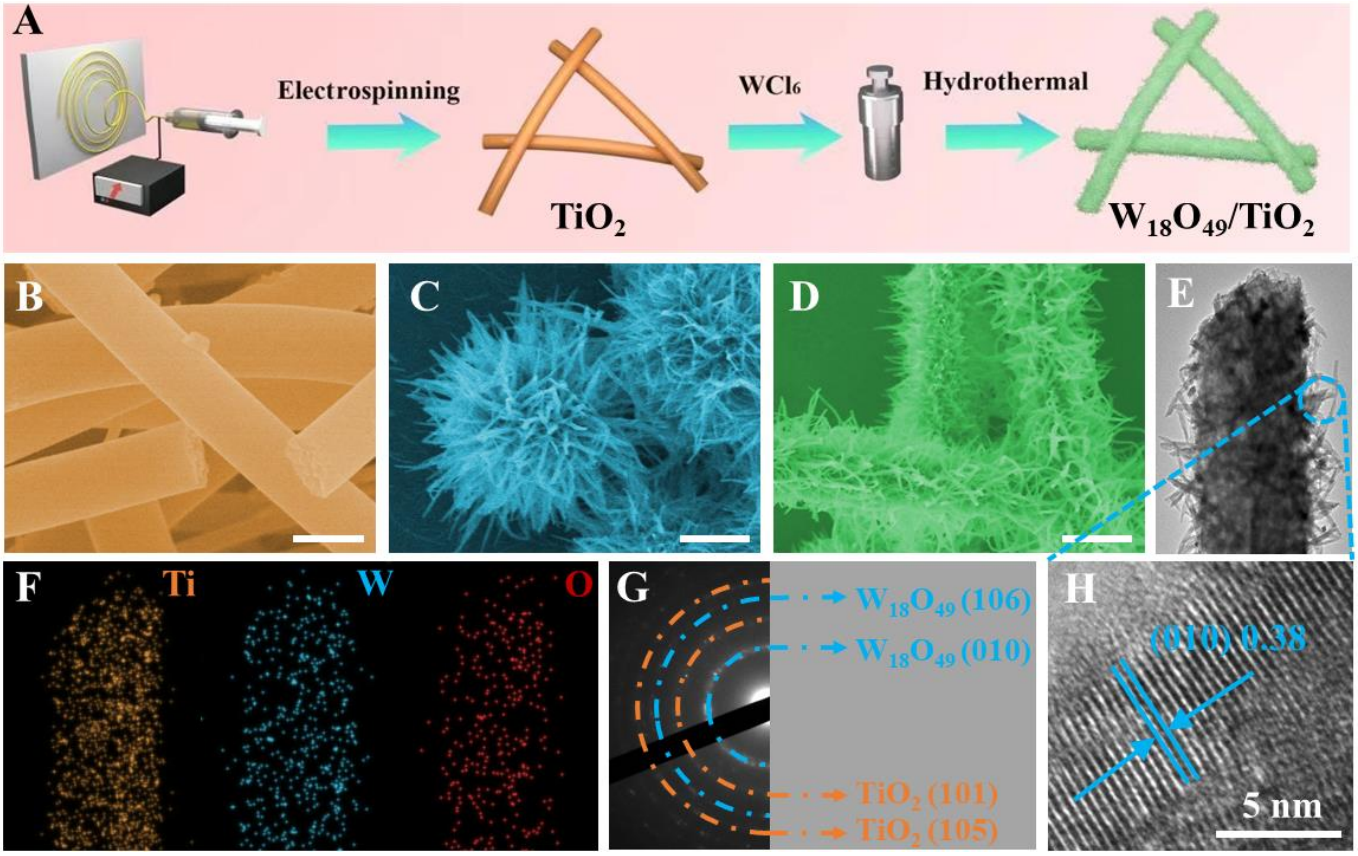

Figure 1(A) Fabrication process of the $W_{18}O_{49}/TiO_2$ heterostructure; SEM images of (B) TiO_2 nanofibers (NFs), (C) $W_{18}O_{49}$ nanowires (NWs) and (D) $W_{18}O_{49}/TiO_2$ heterostructure, the scale in the Figure is 500 nm; (E) TEM images of an individual $W_{18}O_{49}/TiO_2$ heterostructure; (g) SAED pattern and (h) HRTEM image of the $W_{18}O_{49}/TiO_2$ heterostructure.

This journal is © The Royal Society of Chemistry 2023

Please do not adjust margins

create $W_{18}O_{49}$ enables the production of the desired $W_{18}O_{49}/TiO_2$ trunk-branched heterostructure, see Figure S1. The resulting diameters range from 10 to 40 nm and lengths range from 200 to 500 nm. Figure 1D indicates that the surface of the TiO_2 nanofibers became rough after the hydrothermal reaction, and were decorated with high density $W_{18}O_{49}$ NWs which contributed to electron-hole separation to create a highly response device. To further clarify the heterostructure characteristics, we carried out detailed component analysis in Figure 1E and F, where a transmission electron microscopy (TEM) image of an individual $W_{18}O_{49}/TiO_2$ nanofiber and the corresponding spatially-resolved elemental mapping of Ti, W and O elements are presented. These images reveal that Ti is primarily distributed in the middle of the branched trunk heterostructure and W is dominant in the external region of the trunk. It can be seen that the spatial distributions of Ti, W and O elements fit well with the trunk-branched morphologies of a $W_{18}O_{49}/TiO_2$ heterostructure, implying that the branches consist of $W_{18}O_{49}$, whereas the TiO_2 phase is located at the center of the trunk. The corresponding selected area electron diffraction (SAED) pattern can be indexed to two sets of diffraction rings that consist of monoclinic $W_{18}O_{49}$ and anatase TiO_2, see Figure 1G. At a higher magnification, only a lattice stripe of $W_{18}O_{49}$ can be observed in $W_{18}O_{49}/TiO_2$ heterostructure, which confirms the structure of TiO_2 nanofibers with branches of $W_{18}O_{49}$ nanowires attached. The high-resolution transmission electron microscope (HRTEM) analysis in the labeled region of Figure 1E indicates a lattice fringe length of d = 0.38 nm in Figure 1H, which is the response of the {010} planes of the $W_{18}O_{49}$ nanowires.

Energy dispersive spectroscopy (EDS) results and the elemental composition of $W_{18}O_{49}/TiO_2$ are shown in Figure 2A, where W, Ti and O exist. The X-ray diffraction (XRD) pattern reveals no new peaks, apart from the characteristic peaks of individual components, suggesting the solvothermal preparation creates a truly hierarchical heterostructure (see Figure 2B). The element chemical state and binding environment of $W_{18}O_{49}/TiO_2$ heterostructures are examined by X-ray photoelectron spectroscopy (XPS). Figure 2C shows the $W_{18}O_{49}/TiO_2$ branched heterostructures with a binding energy from 0 to 800 eV. The XPS spectrum demonstrates the existence of W, Ti, and O elements, which are consistent with the EDS element distribution map. As shown in Figure 2D, strong characteristic peaks are clearly observed, which are assigned to Ti $2p_{3/2}$ (458.7 eV) and Ti $2p_{1/2}$ (464.4 eV), which is the normal state of Ti^{4+} in the trunk of $W_{18}O_{49}/TiO_2$ heterojunction [29]. For the $W_{18}O_{49}/TiO_2$ heterojunction, there are two kinds of W states, including four symmetric peaks in the W 4f region. The peaks at 34.1 eV and 35.5 eV originate from W $4f_{7/2}$, and the peaks at 36.7 eV and 37.6 eV are attributed to W $4f_{5/2}$. These indicate that W^{5+} and W^{6+} exist in the $W_{18}O_{49}$ nanowire branches, which is in agreement with reports on plasmonic semiconductor tungsten oxides, as shown in Figure 2E [30]. The results further confirm the existence of non-stoichiometric W atoms, accompanied by the appearance of oxygen vacancies. To study the chemical state, the O 1s peaks of XPS spectra can be well fitted by three peaks, see Figure 2F. The peak at 530.3 eV corresponds to a O 1s level of the O^{2-} oxygen atom in the $W_{18}O_{49}/TiO_2$ heterojunction. The peaks at 532.68 eV and 531.38 eV are assigned to the hydroxyl group (OH^-) on the oxide surface and the chemisorbed oxygen species, respectively. The XPS

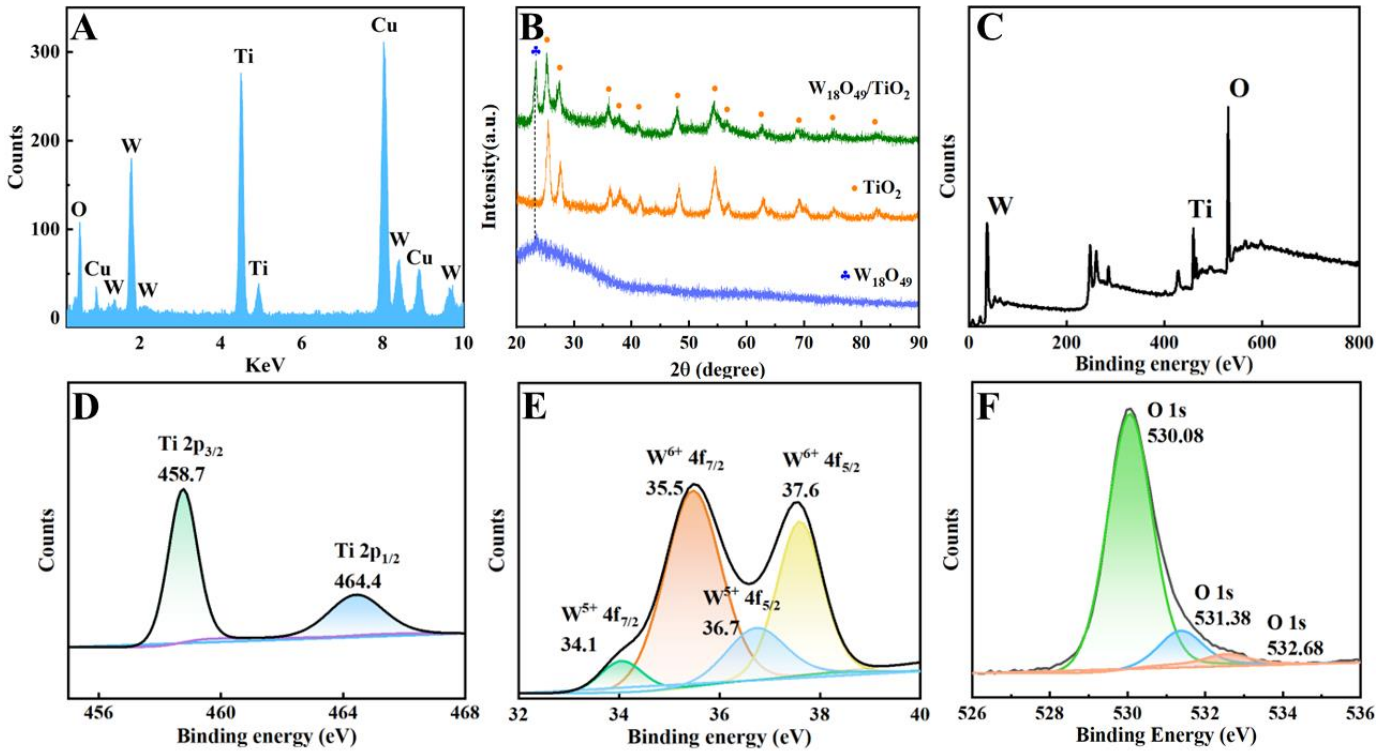

Figure 2 (A) EDX spectra of $W_{18}O_{49}/TiO_2$; (B) XRD patterns of the as-fabricated samples: Orange is TiO_2, blue is $W_{18}O_{49}$, green is $W_{18}O_{49}/TiO_2$; (C) XPS spectrum of the $W_{18}O_{49}/TiO_2$ heterostructure: (D) Ti 2p core-level spectrum; (E) W 4f core-level spectrum; (F) O 1s core-level spectrum.

Please do not adjust margins

analysis shows that there are abundant oxygen vacancies, which can greatly improve the light absorption performance by moving the Fermi level up and promoting carrier separation by accelerating the surface reduction half reaction [31, 32].

As a classic "optical antenna", plasmonic nanostructures, with the unique capability to amplify the incident light intensity, strongly depend on the shape, size and position of the heterojunction system. Figure 3A reveals the broad plasmonic extinction band of $W_{18}O_{49}$ nanowires in the wavelength range from 325 nm to 800 nm. When combined with finite element modelling (FEM), we demonstrate the directional dependence and intensity distribution of the localized electric field of the $W_{18}O_{49}$ nanowires. The extinction signal prior to 445 nm of the mode of the electric field is dominant. Similar to a typical 1D noble metal nanostructure (e.g., nanowire, or nanorod) with two resonance modes [33], Figure 3B shows that the single nanowire model system can describe the optical properties with respect to the electric field directions (i.e., transverse [E_T, as indicated by the red arrow], longitudinal [E_L, as indicated by the blue arrow] and incident light [*k*, as indicated by the black arrow]); the contour color indicates the electric field enhancement, $|E|^2/|E_0|^2$. The transverse plasmon mode is generated by electron oscillations perpendicular to the principal axis of the $W_{18}O_{49}$ nanowires; see Figure 3B. For the longitudinal plasmon mode, electrons oscillate along the principal axis of nanowire, and the plasmon propagates horizontally in the

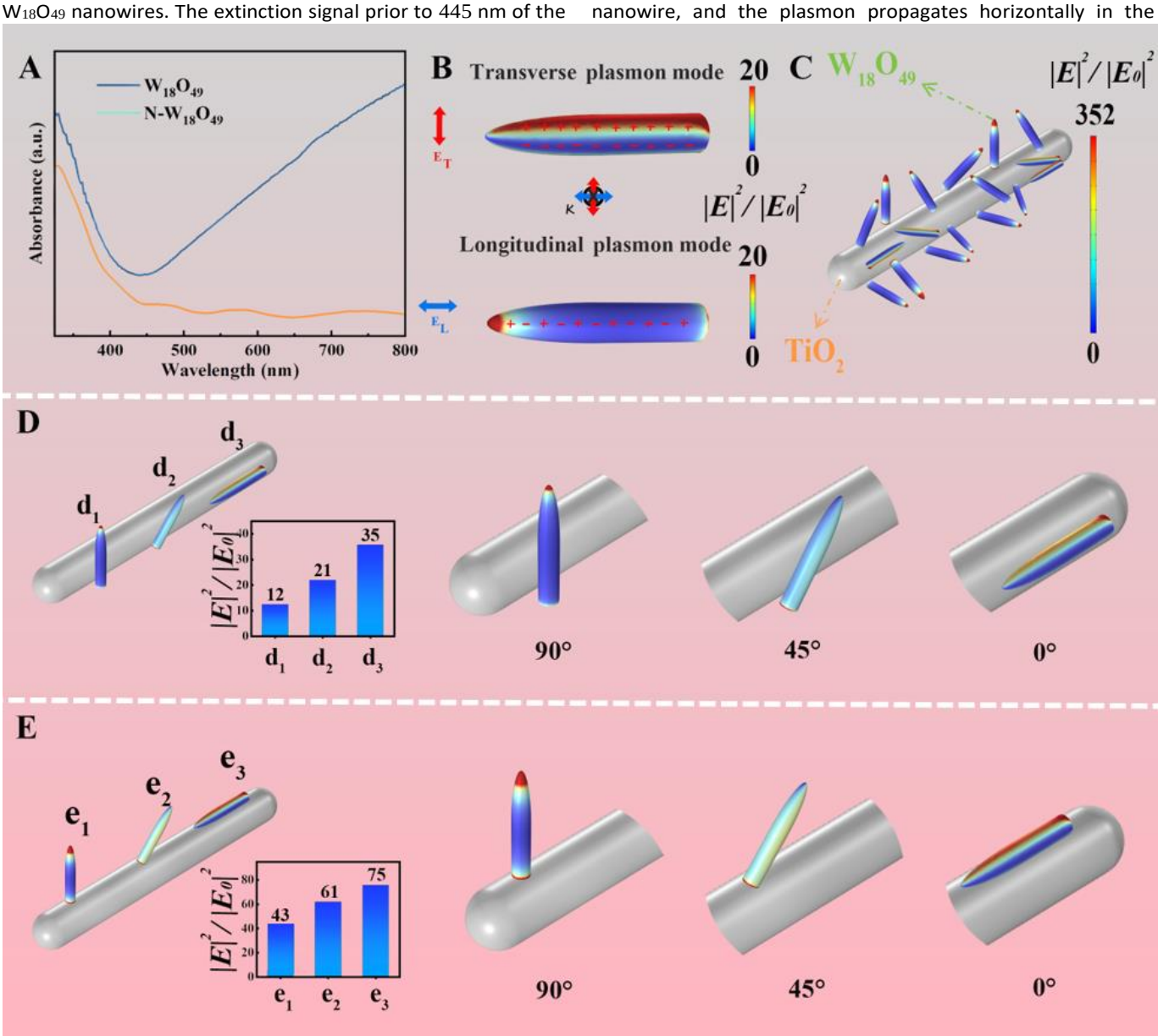

Figure 3(A) UV-vis-IR absorption spectra of the $W_{18}O_{49}$ and N-$W_{18}O_{49}$; Electric field distributions with incident irradiation of 375 nm of (B) single $W_{18}O_{49}$ nanowire with respect to the electric field directions (transverse [E_T] and longitudinal [E_L] directions), *k* (black arrow) indicates the direction of the incident light; (C) Electric field distributions of the isolated $W_{18}O_{49}$/TiO_2 nanofiber and a single $W_{18}O_{49}$ nanowire and TiO_2 nanofiber at different contact positive: (D) *tip contact* and (E) *cross contact*, under incident irradiation (375 nm) along the z-axis.

$W_{18}O_{49}$ nanowires, see Figure 3A, is primarily due to the transverse plasmon mode, whereas in the long-wavelength range (> 445 nm), the extinction spectrum of the longitudinal nanowire. Unlike the transverse plasmon mode of noble metal, the short-wavelength extinction (< 445 nm) of the $W_{18}O_{49}$ nanowires originates from two aspects. Firstly, the existence of

This journal is © The Royal Society of Chemistry 2023

Please do not adjust margins

intrinsic absorption in $W_{18}O_{49}$ can be confirmed through the extinction spectrum of N-$W_{18}O_{49}$, where the intensity clearly weakens but is still present and the $W_{18}O_{49}$ that loses its plasmonic properties is defined as N-$W_{18}O_{49}$ (Figure 3A), which are formed through H_2O_2 treatment of plasmonic $W_{18}O_{49}$ to passivate their surface oxygen vacancies. Secondly, for the transverse plasmon mode, the extinction intensity of N-$W_{18}O_{49}$ is lower than that of the $W_{18}O_{49}$ and suggests the contribution of the transverse plasmon resonance effect. This statement is also supported by localized electric field enhancement of the transverse plasmon mode when the incident direction is perpendicular to the principal axis, see Figure 3B. Due to the coupling between the transverse plasmonic extinction wavelength and excitation light of 375 nm, this leads to an enhancement compared to the longitudinal electric field. As shown in Figure 3C, the random contact model of $W_{18}O_{49}/TiO_2$ displays a significant localized field enhancement (up to 352-fold) and a plasmon coupling effect between nanowires which mainly occurs in the contact region of two domains ($W_{18}O_{49}$ and TiO_2).

To reveal the localized electric field in the $W_{18}O_{49}/TiO_2$ heterojunction, the relative positions of the $W_{18}O_{49}$ and TiO_2 domains are displayed in Figure 3C. We now simplify the heterojunction into two contact types of a single $W_{18}O_{49}/TiO_2$ heterostructure; namely (i) *cross contact* (as in Figure 3D), where the side of the $W_{18}O_{49}$ nanowire contacts the side surface of the TiO_2 nanostructure and (ii) *tip contact* (Figure 3E), where the tip of the $W_{18}O_{49}$ nanowire contacts the front of the TiO_2 nanostructure; these are both further refined into contacts at different angles: 90°, 45° and 0°, as shown in Figure 3D and E respectively, where the maximum field enhancement is shown. It can be seen that the *tip contact* type (Figure 3E) experiences a more intense electric field based on the high electron density at the tip. The electric field enhancement of the tip contact mode (Figure 3E) exceeds that of the *cross contact* mode for all contact angles (Figure 3D). In the case of the tip of $W_{18}O_{49}$ nanowire making contact with the long axis (z-axis) of TiO_2 at different angles, the maximum electric field enhancement value reaches 43 (Figure 3e$_1$), 61 (Figure 3e$_2$) and 75 (Figure 3e$_3$) around the surface nanostructure, respectively. We observe an increase of $|E|^2/|E_0|^2$ in the 0° parallel contact model (Figure d$_1$, e$_1$), as compared to a 45° (Figure d$_2$, e$_2$) or 90° contact mode (Figure d$_3$, e$_3$), where the optimum strength lies in the *tip contact* type, rather than the *cross contact* (see Figure 3D and E). Therefore, it is confirmed that the localized electric field distribution induced by a plasmon resonance effect is relevant to the contact mode in $W_{18}O_{49}/TiO_2$ heterojunction system under 375 nm excitation, which consequently enhances the extinction performance of the scattering effect of incident light. It should be noted that the electric field enhancement mainly emerges in the vicinity of $W_{18}O_{49}/TiO_2$ trunk-branch heterostructures. These results illustrate that the LSPR-induced by incident light can be strongly concentrated and magnified via the plasmonic $W_{18}O_{49}$ branches near the TiO_2 trunk. In general, the enhanced localized electric field at the heterogenous interface is accompanied by the generation of "hot electrons" and increase of localized temperature [34]. Thus, similar to a photoelectric system that is modulated by a noble metal [35], it is reasonable to suggest that the $W_{18}O_{49}$ loaded on the TiO_2 favors both the kinetic process of producing plasmonic "hot electrons"

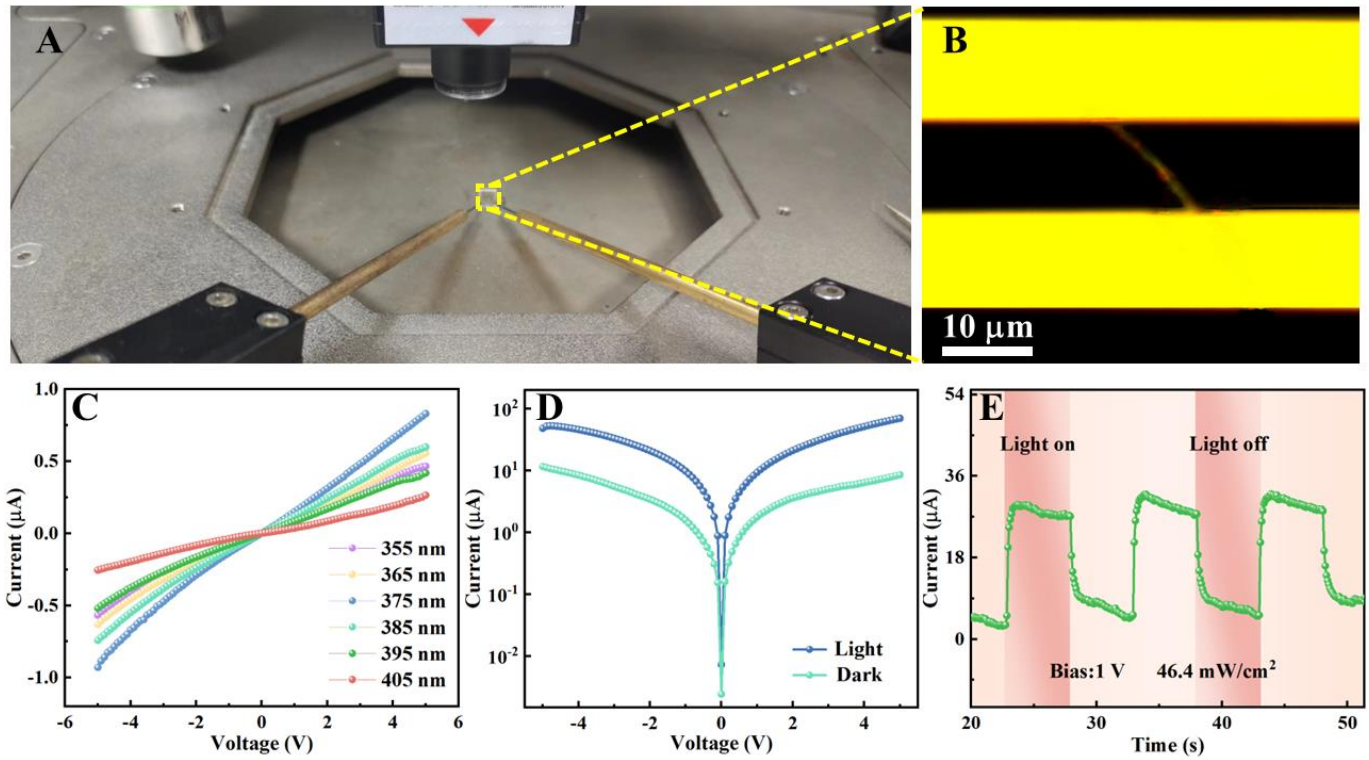

Figure 4(A) Photograph showing the property measurements of the fabricated photodetectors conducted on a four-probe station; (B) Corresponding microphotograph of single nanofiber photodetector; (C) *I-V* characteristic curves of $W_{18}O_{49}/TiO_2$ photodetectors under di fferent wavelengths irradiation with 1 V bias voltage; (D) Logarithmic *I-V* curves and (E) *I-T* characteristic curves of single $W_{18}O_{49}/TiO_2$ heterostructure under irradiation 375 nm.

Please do not adjust margins

Please do not adjust margins

and a thermal effect, thereby leading to a synergistic photo/thermal photoelectric response under UV-light.

We now undertake functional $W_{18}O_{49}/TiO_2$ photodetector performance using a four-probe station in conjunction with a semiconductor characterization system, see Figure 4A. Figure 4B shows a microphotograph of an individual $W_{18}O_{49}/TiO_2$ nanofiber photodetector with an electrode separation of approximately 10 μm. Subsequently, the current-voltage (*I-V*) curves of a single $W_{18}O_{49}/TiO_2$ nanofiber photodetector is measured after irradiation at a range of wavelengths using a 500-W Xenon arc lamp as a light source, see Figure 4C. It can be observed that the current flowing through the photodetector exhibits a linear relationship with an increase of applied biases, suggesting that the contacts are ohmic in nature between the $W_{18}O_{49}/TiO_2$ nanofiber and Au electrodes, which can reduce the contact barriers of the heterojunction system, leading to the enhanced capabilities of the device [36]. By subjecting devices to an appropriate light wavelength state (375 nm at 46.4 mW/cm^2 illumination at 1 V bias originated from Figure 4C) and in the dark, the photoconductive behavior of a single $W_{18}O_{49}/TiO_2$ nanofiber is recorded using the logarithmic *I-V* curves in Figure 4D. This can be ascribed to the effective separation of electron-hole pairs based on absorption of the illumination light, and the transfer of plasmon-induced "hot electrons" to enhance the photoconductive behavior under a bias voltage [26]. Figure 4E shows a typical photo-switching characteristic of an individual nanofiber detector measured by periodically turning the 375 nm light of a laser diode on and off under ambient air conditions at a bias of 1.0 V, with an average power of 46.4 mW/cm^2. The photocurrent performance indicates a sharp increase and fall with the irradiation turning on and off, and confirms the as-constructed photodetector exhibits excellent stability and reproducibility.

To consolidate the afore-mentioned results, the specific impact of the plasmon resonance effect on the optoelectronic properties of the photodetector devices with the ultraviolet-light (UV-light) intensities is investigated in Figure 5. The time-response curves of conventional TiO_2 photodetectors and logarithmic *I-V* curves of a $W_{18}O_{49}/TiO_2$ photodetector are measured under illumination at 375 nm with light intensities ranging from 1.4 mW/cm^2 to 57.5 mW/cm^2 at a bias of 1 V. For the TiO_2 photodetector device, a stable photocurrent without evident fluctuation exhibits a rising trend with increasing UV intensity, see Figure 5A. The photocurrent of the plasmonic $W_{18}O_{49}/TiO_2$ photodetector also increases gradually with increasing incident light intensity in Figure 5B, demonstrating that more carriers are transported to the corresponding electrodes at stronger light intensities. A strong proportional relation between the photocurrent and light intensity is clearly observed, and the results in Figure 5C reveal the excellent capability of the $W_{18}O_{49}/TiO_2$ photodetector devices for UV photon utilization. The nonlinear dependence of current-power relation is analyzed by a power law: $I = AP^{\theta}$, where A is a constant for a given wavelength, P is the light intensity, and θ is the exponent denoting that this response of the photocurrent to light intensity presents the generation, recombination, and trapping process of electron-hole within the semiconductor [37]. The θ value of the photodetectors can be estimated with an applied bias of 1 V, which is lower than the idea index value of 1, indicating the existence of trap states in the devices [38].

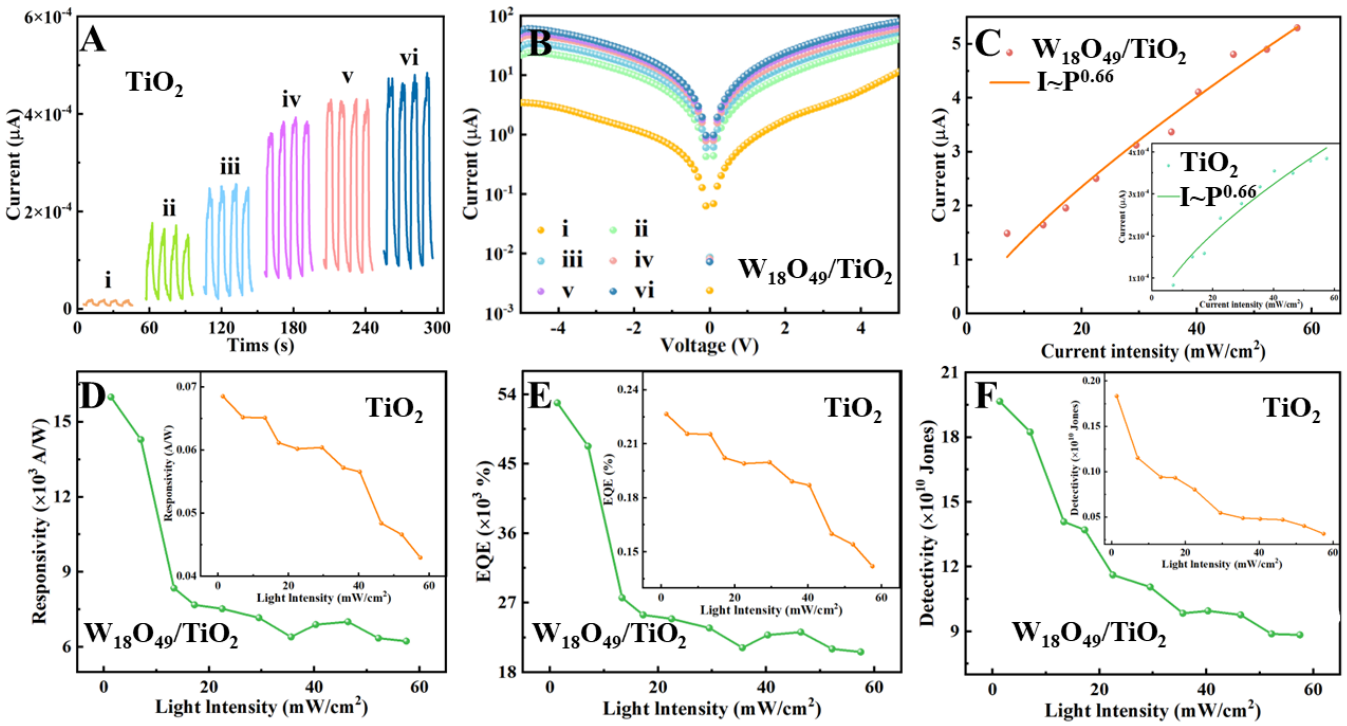

Figure 5(A) Time-response curves of TiO_2 nanofiber photodetector and (B) Logarithmic *I-V* curves of $W_{18}O_{49}/TiO_2$ photodetector irradiated at 375 nm with respect to different intensities: i) 1.4 mW/cm^2; ii) 13.3 mW/cm^2; iii) 22.5 mW/cm^2; iv) 35.6 mW/cm^2; v) 46.4 mW/ cm^2; vi) 57.5 mW/cm^2; (C) Relationship between the photocurrents and light intensities of different photodetectors at a fixed incident-light wavelength of 375 nm; (D) Plots of responsivity, (E) EQE and (F) detectivity of different photodetectors versus light intensities at a bias of 1 V.

This journal is © The Royal Society of Chemistry 2023

Please do not adjust margins

Please do not adjust margins

Meanwhile, the exponent value of $W_{18}O_{49}/TiO_2$ heterostructure (0.77 close to 1) suggests less trap states compared to a purely TiO_2 photodetector ($\theta = 0.66$) [39, 40], which can be related to the plasmonic heterostructure efficiently collecting photoinduced charge carriers in the space charge region [41, 42].

We now carry out a representative optoelectronic performance comparison between a pristine TiO_2 photodetector and a $W_{18}O_{49}/TiO_2$ photodetector under UV light illumination with a 1 V bias. The responsivity (R), external quantum efficiency (EQE) and detectivity (D^*) are three key parameters to evaluate the optoelectronic performance of the photodetector. In this work, the photodetectors are measured at a modulation frequency of 150 Hz, so the low frequency noise ($1/f$) can be ignored and thus the D^* could be calculated using the formula. The parameters can be expressed as the following equations:

$$R_\lambda = \frac{\Delta I}{P_\lambda S} \quad (1)$$

$$EQE = \frac{hc}{e\lambda} \cdot \frac{\Delta I}{P_\lambda S} \quad (2)$$

$$D^* = \frac{R_\lambda}{\left(2e\frac{I_{off}}{A}\right)^{\frac{1}{2}}} \quad (3)$$

where ΔI is the difference between the photocurrent and the dark current, P_λ is the effective incident laser power, A is the effective area of the detector, h is Planck's constant, c is the velocity of light, e is the electronic charge, λ is the exciting wavelength, I_{off} is the dark current and e is the elementary charge. It can be seen from Equations (1-3) that the dark current of a photodetector should be suppressed to the lowest possible level to distinguish weak optical signals and R_λ and EQE are closely related to light intensity. The values of R, EQE and D^* are plotted as a function of different P_λ of 375 nm light illumination for both the TiO_2 and $W_{18}O_{49}/TiO_2$ photodetectors in Figure 5 D-F, and the maximum calculated, and values of the $W_{18}O_{49}/TiO_2$ photodetector are $R = 1.6 \times 10^4$ A/W, EQE = 5.29×10^4 % and $D^* = 1.97 \times 10^{11}$ cm $Hz^{1/2}$ W^{-1} for $\lambda = 375$ nm, $P = 1.4$ mW/cm^2, and $V_{bias} = 1$ V. Correspondingly, the obtained highest R and EQE values for the $W_{18}O_{49}/TiO_2$ photodetector device are enhanced by a factor of 10^5 times compared to those of the TiO_2 photodetector, while the D^* value of the $W_{18}O_{49}/TiO_2$ photodetector is 100 times that of the TiO_2 photodetector due to the associated increase in dark current. These results imply that the plasmonic $W_{18}O_{49}$ can effectively facilitate the charge separation and enhance light absorption through the heterogenous interfacial charge transfer process and/or LSPR behavior, which can be integrated in a low-cost non-metallic heterostructure. In addition, the calculated R, EQE and D^* values of the two photodetector devices exponentially decrease as the power intensity increases. Under the highest lighting power density, the increased number of photogenerated charge carriers can induce a reverse electric field that opposes the equilibrium built-in field, effectively lowering the built-in electric field in the photodetector system. Thus, the charge carrier recombination at the interface is accelerated with a resulting decrease in optoelectronic performance [43, 44]. This photocurrent saturation phenomenon may be of particular importance in high-dynamic-range sensing to avoid saturation effects at the readout under intense illumination [44]. These parameters, along with the literature values reported for the TiO_2-based photodetectors, are summarized in Table 1. The photoelectric performance of the $W_{18}O_{49}/TiO_2$ photodetector is comparable to the other state-of-the-art photodetectors. In particular, in terms of responsiveness, our $W_{18}O_{49}/TiO_2$ photodetector is superior to previously reported photodetectors with different structures or strategies; it also exhibits superior capabilities for UV photodetector with an individual 1D nanostructure.

To clarify the influence of the SPR-coupling-induced photothermal effect on the UV light detection, the current-time (I-T) characteristics of single TiO_2 nanofiber photodetector at different temperatures are performed using 375 nm light with a power density of 46.4 mW/cm^2 at a bias of 1.0 V, as shown in Figure 6A. The results demonstrate that the photocurrent increases with an increase of the working temperatures, which mainly originates from the heated electrons with a higher transport speed, resulting in the acceleration of carrier recombination. In view of the raised temperatures, the work

Table 1 Performance Comparisons of Photodetectors with Different Structures or Strategies

Device	Bias (V)	λ (nm)	τ_r (s)	τ_f (s)	R (A/W)	D^* (cm $Hz^{1/2}$ W^{-1})	Ref.
TiO_2/Perovskite	10	400-800	0.49	0.56	0.008	1.9×10^{12}	7
Ag/NiO/TiO_2	0	365	0.004	0.0043	0.2	1.4×10^{10}	42
TiO_2/P_3HT	0	350	0.72	0.5	3.7×10^{-5}	1.6×10^{10}	45
Au/TiO_2/P_3HT	0	350	0.48	2.12	2.5×10^{-4}	2.9×10^{10}	45
TiO_2/Ag	/	350	0.002	0.047	1.1×10^{-3}	/	46
In_2O_3/TiO_2	2	280	2.1	0.3	799.5	1.1×10^{12}	47
Co_3O_4/ TiO_2	5	380	0.17	0.21	4	2.8×10^{11}	48
Ag-TiO_2/RGO	4	350	0.16	0.49	1760	6.7×10^{13}	49
$W_{18}O_{49}/TiO_2$	1	375	0.292	0.245	1.6×10^4	1.97×10^{11}	This work

This journal is © The Royal Society of Chemistry 2023

Please do not adjust margins

Please do not adjust margins

function of the semiconductor and the height of the potential barrier between the electrodes and nanofiber can be reduced, which contributes to the decrease in contact resistance [50]. In addition, the localized temperature may also speed up the adsorption and desorption process of oxygen at surface states [51, 52]. Moreover, the photothermal effect is quantitatively evaluated by using an infrared thermal camera under 375 nm irradiation (see Figure 6B). Monitoring the localized temperature on the surface of the film formed by $W_{18}O_{49}$ nanowires, similar to noble metal nanostructures, the strong localized heating phenomenon occurs from initial temperature 21 ℃ to 77 ℃ after irradiating steadily for 1 min [35, 53]. Furthermore, we employ a N-$W_{18}O_{49}$/TiO_2 to exhibit no LSPR effect as a control sample in order to verify the impact of plasmonic $W_{18}O_{49}$ on the optoelectronic properties. The passivated N-$W_{18}O_{49}$/TiO_2 photodetector is identical to the $W_{18}O_{49}$/TiO_2 photodetector in structural features and component morphology. Figure S2 reveals the equivalent circuit is not influenced by the N-$W_{18}O_{49}$ in the photodetector system produced. Importantly, the observation reveals that the *I-T* characteristic behavior of N- $W_{18}O_{49}$/TiO_2 with a filled oxygen vacancy is much lower than plasmonic $W_{18}O_{49}$/TiO_2, and is yet higher than TiO_2 due to the formation of a non-plasmonic heterostructure that retains and improves photoprobe performance. Thus, the results demonstrate our heterojunction photodetector system $W_{18}O_{49}$/TiO_2 possesses a beneficial working temperature, suggesting the synergetic coupling effect between plasmonic "hot electrons" and a LSPR-induced photothermal in the as-fabricated plasmonic photodetector to promote the photoelectric properties. This internal heating characteristic under room temperature and low voltage (1 V) offers more possibilities for detection of UV light at low temperatures.

Figure 6C presents the temporal response of the $W_{18}O_{49}$/TiO_2 photodetector device, which are defined as the photocurrent reaching 90% of the highest value (termed *rise time* τ_r) and a drop to 10% (termed *recovery time* τ_f) [54,55]. Under 375 nm illumination, the rise time and recovery time of the heterostructure photodetector can be estimated to be 0.265 s and 0.197 s, respectively. It is verified that the rise and recovery times of TiO_2 photodetector are significantly slower than those of the composite counterpart (see Figure S3). For $W_{18}O_{49}$/TiO_2 photodetector, the photo response of the device could be mainly attributed to the spatial separation of photo-generated electrons from TiO_2 to $W_{18}O_{49}$, the generation and fast transfer of "hot electrons" induced by surface plasmon resonance to overcome the carrier cooling and trapping process[56, 57]. As we can see, the photocurrent shows a trend of decreasing and then leveling off with laser irradiation. This is mainly due to once the 375 nm UV laser is suddenly subjected for irradiation, the localized temperature (dT/dt >0) of $W_{18}O_{49}$/TiO_2 photodetector would be rapidly raised, due to the LSPR-induced photothermal effect. In this case, the direction of the current generated by the photothermal effect is like to that of the photocurrent generated by the photovoltaic effect, accounting for the sharp increased current at the moment of turn-on light. When the UV light is continuously irradiated, the temperature of the photodetector reaches a constant value, implying that the output current is lowered, followed by maintaining at a stable plateau. To demonstrate its stability, the photocurrents of a single $W_{18}O_{49}$/TiO_2 photodetector are monitored over the course of a day under irradiation by 375 nm light, see Figure 6D.

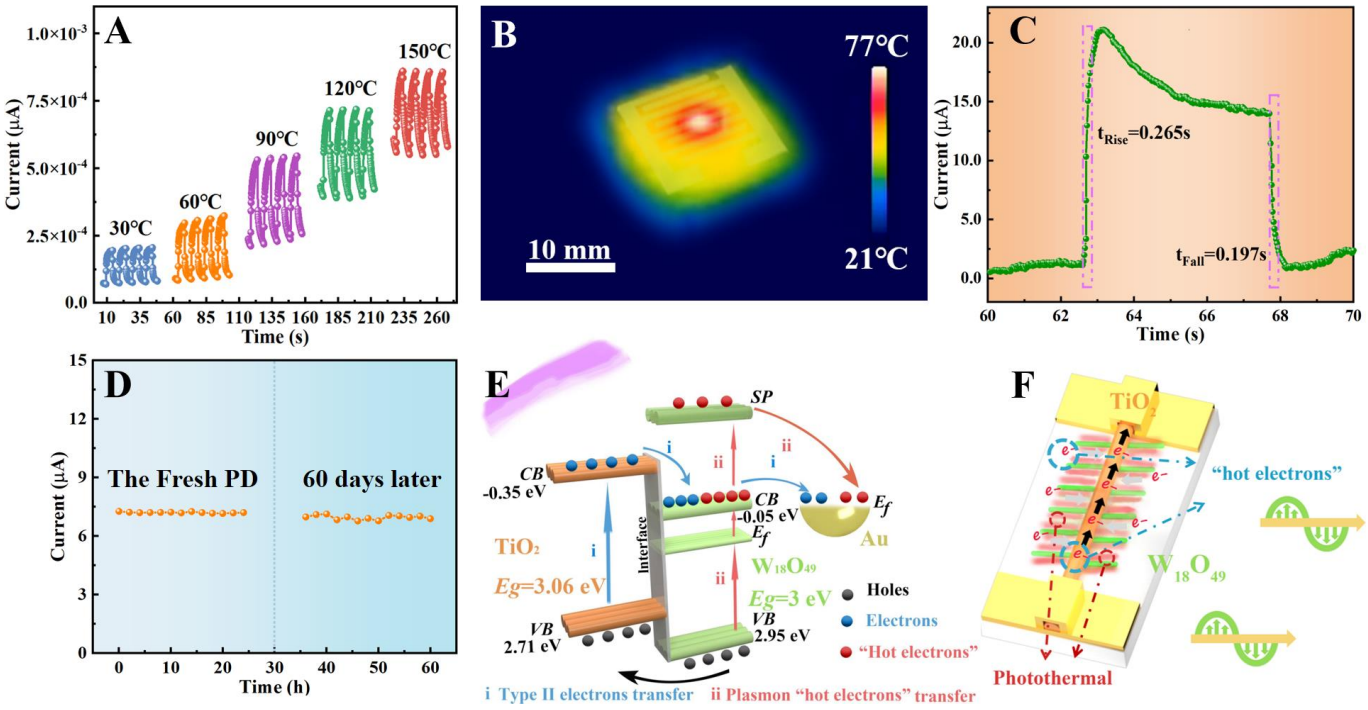

Figure 6(A) *I-T* characteristic curves of TiO_2 photodetector at different temperatures; (B) Infrared thermal photographs of $W_{18}O_{49}$/TiO_2 photodetectors; (C) *I-T* characteristic curves of the $W_{18}O_{49}$/TiO_2 photodetectors; (D) Long-term stability of as-constructed $W_{18}O_{49}$/TiO_2 photodetectors under room temperature; (E) Schematic of the kinetics process of the interfacial electron transfer in the $W_{18}O_{49}$/TiO_2 heterostructures; (F) Schematic for the as-constructed photodetector nanodevice based on a single $W_{18}O_{49}$/TiO_2 trunk-branched heterostructures.

This journal is © The Royal Society of Chemistry 2023

Please do not adjust margins

Please do not adjust margins

We now take a new single $W_{18}O_{49}/TiO_2$ nanofiber photodetector device, and the corresponding photocurrents could remain almost the same as the initial value with a negligible fluctuation amplitude of below 1%. Interestingly, for a photodetector which has been preserved under ambient conditions for one month, these photocurrents exhibit small fluctuation amplitudes of below 5.1%. These factors describe the long-term stability of the nanofiber photodetector device during operation under an air environment. The spatial kinetic behavior of the photon-generated carriers across the interface is primarily defined by the energy band configuration in heterojunction photodetector system. It is therefore necessary to understand the effects of both "hot electrons" transfer and photothermal effects of plasmonic $W_{18}O_{49}$ on the enhanced optoelectronic characteristic. Figure S4 provides the UV-vis-IR absorption spectra of TiO_2 nanofibers and $W_{18}O_{49}$ nanowires, illustrating that the bandgap with semiconductive properties are ≈ 3.06 eV and ≈ 3.00 eV, respectively. The semiconductor nature and band structure of $W_{18}O_{49}/TiO_2$ are further studied by Mott-Schottky plots, where Figure S4c shows a positive slope in both TiO_2 and $W_{18}O_{49}$, corresponding to the n-type semiconductor characteristics. The flat band potentials (E_{fb}) of TiO_2 and W18O49 are estimated to be approximately -0.45 V and -0.15 V (vs Ag/AgCl, pH ≈ 7) through the intersection of the tangent line with the x-axis. According to the Nernst equation, the measured flat band potential (vs. NHE) is equivalent to -0.25 V and 0.05 V, thus the conduction band potential (E_{CB}) could be converted to -0.35 V and -0.05 V due to the conduction band (*CB*) potential is negative about ~0.1 V than their flat band potential for n-type semiconductor [58, 59]. For both TiO_2 and $W_{18}O_{49}$, it can be observed that the valence band (E_{VB}) can be determined to be +2.71 V and +2.95 V (vs. NHE), by the formula ($E_g = E_{VB} - E_{CB}$), respectively. Based on the afore-mentioned experimental results, a schematic of the possible energy band positions and the proposed interfacial electron transfer process over the as-constructed photodetector nanodevices based on a single $W_{18}O_{49}/TiO_2$ trunk-branched heterostructures are demonstrated in Figure 6E. Under UV light irradiation, there are two possible electron kinetic transfer processes, and both TiO_2 and $W_{18}O_{49}$ can effectively produce electrons and holes due to their respective absorption of UV region. Firstly, there is a traditional Type II heterogeneous electron transfer. Given the Type II heterojunction formed at the interface, the electrons in the conduction band (*CB*) of TiO_2 can rapidly move to the *CB* of $W_{18}O_{49}$ and then transfer to the Au electrodes, promoting carrier separation while the holes transfer from the VB of $W_{18}O_{49}$ to the VB of TiO_2. Secondly, there is a plasmonic "hot electrons" surface plasmon (*SP*) state electron transfer. Upon LSPR excitation, the excess free electrons around the Fermi level of $W_{18}O_{49}$ branches can reach the virtual high-energy SP state to form plasmonic "hot electrons". Subsequently, the "hot electrons" can inject into the Fermi level of Au electrodes to cause the LSPR-enhanced photoelectric response [60]. This indicates that the plasmonic heterostructure can increase the optoelectronic performance of TiO_2 based on type II heterogeneous electrons transfer and plasmon "hot electrons" transfer process, which is consistent with the experimental results and uncovers the underlying mechanism of superior performance of heterostructure.

We propose that the photoelectric mechanism (Figure 6F) for this high performance of the single $W_{18}O_{49}/TiO_2$ photodetector device which is primarily attributed to the following four aspects: i) The rational integration of plasmonic $W_{18}O_{49}$ with TiO_2 nanofibers constructs a new generation of plasmonic heterostructure photodetector to strongly enhance the spatial separation of photon-generated carriers and improve the optoelectronic performance; ii) the heavily doped semiconductor $W_{18}O_{49}$ shows an intense LSPR absorption in a wide region. Upon light excitation, the $W_{18}O_{49}/TiO_2$ heterostructure interface experiences collective oscillations of excessive free carriers, which can promote a high localized electric field enhancement; iii) the plasmonic $W_{18}O_{49}$ can absorb the resonance wavelength to induce the generation of "hot electrons", leading to overcome the contact barrier and transfer to the Au electrodes. This injection process is the dominating factor for making a faster transport path for significantly increasing the photocurrent and *R* value; iv) The LSPR-induced the photothermal effect also contributes to reduce the potential barrier and speed up the O_2 desorption process on the surface of heterostructures, thereby desired localized temperature is beneficial to the decrease in contact resistance for the photodetector device.

Conclusions

We have demonstrated the fabrication of a new form of efficient 1D nanofiber heterojunction photodetector based on $W_{18}O_{49}/TiO_2$ nanofibers that are formed via electrostatic spinning, followed by in-situ hydrothermal growth process. By combining detailed experimental characterization with 3D simulations, it is confirmed that the resonance excitation of $W_{18}O_{49}$ nanowires in the as-synthesized heterostructures can greatly magnify the localized electric field from incident light. This new strategy integrates both photo-induced "hot electrons" and a photothermal effect to significantly enhance light absorption and effectively promote carrier separation. The plasmonic $W_{18}O_{49}/TiO_2$ photodetector possesses a maximum responsivity (*R*), external quantum efficiency (EQE) and detectivity (D*) of $R = 1.6 \times 10^4$ A/W, EQE = 5.29×10^4 % and D* = 1.97×10^{11} cm $Hz^{1/2}$ W^{-1} when illuminated by 375 nm light with a power density of 1.4 mW/cm^2 at a bias of 1 V. The photodetector exhibits a significantly improved responsivity, which is five times higher than the pure TiO_2 analogue and significantly exceeds the TiO_2-based photodetectors reported to date. Compared with current reported nanomaterial-based photodetectors, the use plasmonic semiconductor also provide unique advantages, including thermal and environmental stability, when used as the functional units. The present work therefore provides new insights in the exploration of advanced localized surface plasmon resonance (LSPR)-induced photodetectors, with potential applications in future optoelectronic devices.

Please do not adjust margins

Please do not adjust margins

Author Contributions

Conceptualization: Y.Y.; data curation: L.X.Z.; formal analysis: L.X.Z., Y.Y., H.L.Y., Y.H.; funding acquisition: Y.Y., W.Y.Y.; investigation: Y.Y., L.X.Z., Z.S.; validation: L.X.Z., Z.S., T.X.L.; project administration: Y.Y, F.H., W.Y.Y.; software: Z.S., L.X.Z., Z.Z.X.; supervision: L.J., F.H.; writing – original draft: L.X.Z., Y.Y.; writing–review & editing: all authors.

Conflicts of interest

The authors declare that they have no known competing financial interests or personal relationships that could have appeared to influence the work reported in this paper.

Acknowledgements

This work was supported by the National Natural Science Foundation of China (NSFC, Grant No. 62205165) and the College Students Science and Technology Innovation Activity Plan of Zhejiang Province (Grant No. 2022R428A009).

Notes and references

1 M. Isser, H. Kranebitter, E. Kuhn, W. Lederer, High-energy visible light transparency and ultraviolet ray transmission of metallized rescue sheets, *Sci. Rep.*, 2019, **9**, 11208.
2 M. Ichihashi, M. Ueda, A. Budiyanto, T. Bito, M. Oka, M. Fukunaga, K. Tsuru, T. Horikawa, UV-induced skin damage, *Toxicology*, 2003, **189**, 21-39.
3 M.A. Mainster, P.L. Turner, Ultraviolet-B phototoxicity and hypothetical photomelanomagenesis: intraocular and crystalline lens photoprotection, *Am. J. Ophthalmol*, 2010, **149**, 543-9.
4 C.H. Kang, I. Dursun, G. Liu, L. Sinatra, X. Sun, M. Kong, J. Pan, P. Maity, E.N. Ooi, T.K. Ng, O.F. Mohammed, O.M. Bakr, B.S. Ooi, High-speed colour-converting photodetector with all-inorganic CsPbBr3 perovskite nanocrystals for ultraviolet light communication, *Light Sci. Appl.*, 2019, **8**, 94.
5 X. Zhou, C. Wang, J. Luo, L. Zhang, F. Zhao, Q. Ke, High-performance self-powered UV photodetector based on CuI/$CsCu_2I_3$/GaN heterojunction, *Chem. Eng. J.*, 2022, **450**, 136364.
6 M. Haras, T. Skotnicki, Thermoelectricity for IoT – A review, *Nano Energy*, 2018, **54**, 461-476.
7 X. Yi, Z. Ren, N. Chen, C. Li, X. Zhong, S. Yang, J. Wang, TiO_2 Nanocrystal/Perovskite Bilayer for High-Performance Photodetectors, *Adv. Electron. Mater.*, 2017, **3**, 1700251.
8 Y. Cai, L. Tang, J. Xiang, R. Ji, S.K. Lai, S.P. Lau, J. Zhao, J. Kong, K. Zhang, High performance ultraviolet photodetectors based on ZnO nanoflakes/PVK heterojunction, *Appl. Phys. Lett.*, 2016, **109**, 073103.
9 E.V. Gorokhov, A.N. Magunov, V.S. Feshchenko, A.A. Altukhov, Solar-blind UV flame detector based on natural diamond, Instrum. *Exp. Tech.*, 2011, **51**, 280-283.
10 Y. Yao, Z. Li, Y. Han, L. Xie, X. Zhao, Z. Zhu, Fabrication and Characterization of a MnO_2/$Ti_3C_2T_x$ Based Gas Sensor for Highly Sensitive and Selective Detection of Lung Cancer Marker Hexanal, *Chem. Eng. J.*, 2023, **451**, 139029.
11 C.H. Yang, M.C. Lu, H.Y. Lin, G.Z. Lu, Y.F. Chen, A pH-value sensitive and self-powered photodetector based on an anthocyanin/graphene heterojunction, *J. Mater. Chem. C*, 2023.
12 H. Lee, T.Y. Lee, Y. Park, K.S. Cho, Y.G. Rho, H. Choo, H. Jeon, Structurally engineered colloidal quantum dot phosphor using TiO_2 photonic crystal backbone, *Light Sci. Appl.*, 2022, **11**, 318.
13 G. Ycas, F.R. Giorgetta, E.Baumann, I. Coddington, D. Herman, S.A. Diddams, N.R. Newbury, High-coherence mid-infrared dual-comb spectroscopy spanning 2.6 to 5.2 µm, *Nature Photonics*, 2018, **12**, 202-208.
14 L. Yan, S. Tian, M. Weiliang, Y. Wenzhi, S.B. Nanjunda, L. Shaojuan, B. Qiaoliang, Highly responsive broadband black phosphorus photodetectors, *Chin. Opt. Lett.*, 2018, **16**, 020002.
15 L. Colace, G. Assanto, D. Fulgoni, L. Nash, Near-Infrared p-i-n Ge-on-Si Photodiodes for Silicon Integrated Receivers, *J. Light. Technol.*, 2008, **26**, 2954-2959.
16 J.N. Duan, J. Xi, B. Jiao, J.F. Dai, Y.Q Zua, Z.X. Wu, Highly efficient blue emitting one dimensional lead-free nanocrystals, *J. Mater. Chem. C*, 2022, **10**, 11323.
17 S. Quan, S. Guo, D. Weller, S. Fu, Y. Wang, R. Liu, Air-Stable GaSe/ReS_2 Heterojunctions for Self-Powered Polarization-Sensitive Photodetectors, *ACS Appl. Nano Mater.*, 2022, **5**, 7365-7372.
18 C.S.R. Kolli, V. Selamneni, B.A, M.i. Martínez, A.F. Carreno, D. E. Sanchez, M. Terrones, E. Strupiechonski, A.D.L. Bugallo, P. Sahatiya, Broadband, Ultra-High-Responsive Monolayer MoS_2/SnS_2 Quantum-Dot-Based Mixed-Dimensional Photodetector, *ACS Appl. Mater. Interfaces*, 2022, **14**, 15415-15425.
19 Z.L. Deng, T. Shi, A. Krasnok, X. Li, A. Alu, Observation of localized magnetic plasmon skyrmions, *Nat. Commun.*, 2022,**13**, 8.
20 D.H. Lin, F. Wan, S.C. Gong, C. Fu, F.X. Liang, L.B. Luo, A dual-band graphene/silicon nanowire array heterojunction photodetector induced by leaky mode resonances, *J. Mater. Chem. C*, 2023.
21 Z. Liu, F. Li, S. Li, C. Hu, W. Wang, F. Wang, F. Lin, H. Wang, Fabrication of UV Photodetector on TiO_2/Diamond Film, *Sci. Rep.*, 2015, **5**, 14420.
22 P. Zilio, M. Dipalo, F. Tantussi, G.C. Messina, F. de Angelis, Hot electrons in water: injection and ponderomotive acceleration by means of plasmonic nanoelectrodes, *Light Sci. Appl.*, 2017, **6**, e17002.
23 B.Y. Zheng, H. Zhao, A. Manjavacas, M. McClain, P. Nordlander, N.J. Halas, Distinguishing between plasmon-induced and photoexcited carriers in a device geometry, *Nat. Commun.*, 2015, **6**, 7797.
24 A. Manjavacas, J.G. Liu, V. Kulkarni, P. Nordlander, Plasmon-Induced Hot Carriers in Metallic Nanoparticles, *ACS Nano*, 2014, **8**, 7630–7638.
25 Y. Zhang, X. Wang, Y. Zhou, H. Lai, P. Liu, H. Chen, X. Wang, W. Xie, Highly Sensitive and Ultra-Broadband VO_2(B) Photodetector Dominated by Bolometric Effect, *Nano Lett.*, 2022, **22**, 485-493.
26 H. Liu, Y. Liu, S. Dong, H. Xu, Y. Wu, L. Hao, B. Cao, M. Li, Z. Wang, Z. Han, K. Yan, Photothermoelectric SnTe Photodetector with Broad Spectral Response and High On/Off Ratio, *ACS Appl. Mater. Interfaces*, 2020, **12**, 49830-49839.
27 X. Chen, Y. Chen, M. Yan, M. Qiu, Nanosecond Photothermal Effects in Plasmonic Nanostructures, *ACS Nano*, 2012, **6**, 2550–2557.
28 H. Hou, L. Wang, F. Gao, G. Wei, B. Tang, W. Yang, T. Wu, General strategy for fabricating thoroughly mesoporous nanofibers, *J. Am. Chem. Soc.*, 2014, **136**, 16716-9.
29 V.Q. Hieu, T.C. Lam, A. Khan, T.T. Thi Vo, T.Q. Nguyen, V.D. Doan, D.L. Tran, V.T. Le, V.A. Tran, TiO_2/Ti_3C_2/g-C_3N_4 ternary heterojunction for photocatalytic hydrogen evolution, *Chemosphere*, 2021, **285**, 131429.
30 C.H. Shen, X.J. Wen, Z.H. Fei, Z.T. Liu, Q.M. Mu, Novel Z-scheme $W_{18}O_{49}$/CeO_2 heterojunction for improved

This journal is © The Royal Society of Chemistry 2023

Please do not adjust margins

Please do not adjust margins

photocatalytic hydrogen evolution, *J. Colloid Interface Sci.*, 2020, **579**, 297-306.
31 X. Zhou, H.-Y. Zhou, T.-Y. Cheang, Z.-W. Zhao, C.-C. Shen, K. Liang, Y.-N. Liu, Z.-K. Yang, M. Imran, A.-W. Xu, Monodisperse Pd Nanotetrahedrons on Ultrathin MoO_{3-x} Nanosheets as Excellent Heterogeneous Catalyst for Chemoselective Hydrogenation Reactions, *J. Phys. Chem. C*, 2017, **121**, 27528-27534.
32 C.T. Campbell, C.H.F. Peden, Oxygen vacancies and catalysis on ceria surfaces, *Science*, 2005, **309**, 713.
33 W. Xu, T.K. Lee, B.-S. Moon, H. Song, X. Chen, B. Chun, Y.-J. Kim, S.K. Kwak, P. Chen, D.-H. Kim, Broadband Plasmonic Antenna Enhanced Upconversion and Its Application in Flexible Fingerprint Identification, *Adv. Opt. Mater.*, 2018, **6**, 1701119.
34 V.G. Kravets, A.V. Kabashin, W.L. Barnes, A.N. Grigorenko, Plasmonic Surface Lattice Resonances: A Review of Properties and Applications, *Chem. Rev.*, 2018, **118**, 5912-5951.
35 Z. Zhang, X. Jiang, B. Liu, L. Guo, N. Lu, L. Wang, J. Huang, K. Liu, B. Dong, IR-Driven Ultrafast Transfer of Plasmonic Hot Electrons in Nonmetallic Branched Heterostructures for Enhanced H_2 Generation, *Adv. Mater.*, 2018, **30**, 1705221.
36 F. Wang, T. Gao, Q. Zhang, Z.Y. Hu, B. Jin, L. Li, X. Zhou, H. Li, G. Van Tendeloo, T. Zhai, Liquid-Alloy-Assisted Growth of 2D Ternary $Ga_2In_4S_9$ toward High-Performance UV Photodetection, *Adv. Mater.*, 2019, **31**, e1806306.
37 X. Zhang, B. Liu, W. Yang, W. Jia, J. Li, C. Jiang, X. Jiang, 3D-branched hierarchical 3C-SiC/ZnO heterostructures for high-performance photodetectors, *Nanoscale*, 2016, **8**, 17573-17580.
38 P. Xiao, J. Mao, K. Ding, W. Luo, W. Hu, X. Zhang, X. Zhang, J. Jie, Solution-Processed 3D RGO-MoS_2 /Pyramid Si Heterojunction for Ultrahigh Detectivity and Ultra-Broadband Photodetection, *Adv. Mater.*, 2018, **30**, e1801729.
39 L.H. Zeng, M.Z. Wang, H. Hu, B. Nie, Y.Q. Yu, C.Y. Wu, L. Wang, J.G. Hu, C. Xie, F.X. Liang, L.B. Luo, Monolayer graphene/germanium Schottky junction as high-performance self-driven infrared light photodetector, *ACS Appl. Mater. Interfaces*, 2013, **5**, 9362-6.
40 H. Kind, H. Yan, B. Messer, M. Law, P. Yang, Nanowire Ultraviolet Photodetectors and Optical Switches, *Adv. Mater.*, 2002, **14**, 158-160.
41 M. Peng, Y. Tao, X. Hong, Y. Liu, Z. Wen, X. Sun, One-step synthesized PbSe nanocrystal inks decorated 2D MoS_2 heterostructure for high stability photodetectors with photoresponse extending to near-infrared region, *J. Mater. Chem. C*, 2022, **10**, 2236-2244.
42 T.T. Nguyen, M. Patel, S. Kim, R.A. Mir, J. Yi, V.-A. Dao, J. Kim, Transparent photovoltaic cells and self-powered photodetectors by TiO_2/NiO heterojunction, *J. Power Sources*, 2021, **481**, 228865.
43 G. Konstantatos, J. Clifford, L. Levina, E.H. Sargent, Sensitive solution-processed visible-wavelength photodetectors, *Nat. Photonics*, 2007, **1**, 531-534.
44 G. Konstantatos, M. Badioli, L. Gaudreau, J. Osmond, M. Bernechea, F.P. Garcia de Arquer, F. Gatti, F.H. Koppens, Hybrid graphene-quantum dot phototransistors with ultrahigh gain, *Nat. Nanotechnol.*, 2012, **7**, 363-368.
45 L. Zheng, X. Deng, Y. Wang, J. Chen, X. Fang, L. Wang, X. Shi, H. Zheng, Self-Powered Flexible TiO_2 Fibrous Photodetectors: Heterojunction with P_3HT and Boosted Responsivity and Selectivity by Au Nanoparticles, *Adv. Funct. Mater.*, 2020, **30**, 2001604.
46 J. Xu, W. Yang, H. Chen, L. Zheng, M. Hu, Y. Li, X. Fang, Efficiency enhancement of TiO_2 self-powered UV photodetectors using a transparent Ag nanowire electrode, *J. Mater. Chem. C*, 2018, **6**, 3334-3340.
47 A. Moudgil, K.K. Sharma, S. Das, In_2O_3/TiO_2 Heterostructure for Highly Responsive Low-Noise Ultraviolet Photodetector, *IEEE Trans. Electron Devices*, 2020, **67**, 166-172.
48 B. Choudhuri, A. Mondal, S.M.M.D. Dwivedi, M. Henini, Fabrication of novel transparent Co_3O_4 -TiO_2 nanowires p-n heterojunction diodes for multiband photodetection applications, *J. Alloys Compd.*, 2017, **712**, 7-14.
49 P. Deb, J.C. Dhar, Boosted photoresponsivity using silver nanoparticle decorated TiO_2 nanowire/reduced graphene oxide thin-film heterostructure, *Nanotechnology*, 2020,**31**, 285202.
50 A. Varghese, D. Saha, K. Thakar, V. Jindal, S. Ghosh, N.V. Medhekar, S. Ghosh, S. Lodha, Near-Direct Bandgap WSe_2/ReS_2 Type-II pn Heterojunction for Enhanced Ultrafast Photodetection and High-Performance Photovoltaics, *Nano Lett.*, 2020, **20**, 1707-1717.
51 W. Ouyang, F. Teng, X. Fang, High Performance BiOCl Nanosheets/TiO_2 Nanotube Arrays Heterojunction UV Photodetector: The Influences of Self-Induced Inner Electric Fields in the BiOCl Nanosheets, *Adv. Funct. Mater.*, 2018, **28**, 1707178.
52 L. Zheng, K. Hu, F. Teng, X. Fang, Novel UV-Visible Photodetector in Photovoltaic Mode with Fast Response and Ultrahigh Photosensitivity Employing Se/TiO_2 Nanotubes Heterojunction, *Small*, 2017, **13**, 1602448.
53 P. Christopher, H. Xin, A. Marimuthu, S. Linic, Singular characteristics and unique chemical bond activation mechanisms of photocatalytic reactions on plasmonic nanostructures, *Nat. Mater.*, 2012, **11**, 1044-50.
54 D. Zheng, H. Fang, M. Long, F. Wu, P. Wang, F. Gong, X. Wu, J.C. Ho, L. Liao, W. Hu, High-Performance Near-Infrared Photodetectors Based on p-Type SnX (X = S, Se) Nanowires Grown via Chemical Vapor Deposition, *ACS Nano*, 2018, **12**, 7239-7245.
55 X. Zhang, S. Yang, H. Zhou, J. Liang, H. Liu, H. Xia, X. Zhu, Y. Jiang, Q. Zhang, W. Hu, X. Zhuang, H. Liu, W. Hu, X. Wang, A. Pan, Perovskite-Erbium Silicate Nanosheet Hybrid Waveguide Photodetectors at the Near-Infrared Telecommunication Band, *Adv. Mater.*, 2017, **29**, 1604431.
56 Y.F. Chen, Y. Wang, Z. Wang, Y. Gu, Y. Ye, X.L. Chai, J.F. Ye, Y. Chen, R.Z. Xie, Y. Zhou, Z.G. Hu, Q. Li, L.L. Zhang, F. Wang, P. Wang, J.S. Miao, J.L. Wang, X.S. Chen, W. Lu, P. Zhou, W.D. Hu, Unipolar barrier photodetectors based on van der Waals heterostructures, *Nat.Electron.*, 2021, **4**, 357–363.
57 H.Y Wang, Z.X. Li, D.Y. Li, P. Chen, L.J. Pi, X. Zhou, T.Y Zhai, Van der Waals Integration Based on Two-Dimensional Materials for High-Performance Infrared Photodetectors, *Adv. Funct. Mater.*, 2021, **31**, 2103106.
58 Y. Sun, Q. Zhu, B. Bai, Y. Li, C. He, Novel all-solid-state Z-scheme SnO_2/Pt/In_2O_3 photocatalyst with boosted photocatalytic performance on water splitting and 2,4-dichlorophenol degradation under visible light, *Chem. Eng. J.*, 2020, **390**, 124518.
59 X. Hao, Z. Cui, J. Zhou, Y. Wang, Y. Hu, Y. Wang, Z. Zou, Architecture of high efficient zinc vacancy mediated Z-scheme photocatalyst from metal-organic frameworks, *Nano Energy*, 2018, **52**, 105-116.
60 Z. Zhang, J. Huang, Y. Fang, M. Zhang, K. Liu, B. Dong, A Nonmetal Plasmonic Z-Scheme Photocatalyst with UV- to NIR-Driven Photocatalytic Protons Reduction, *Adv. Mater.*, 2017, **29**, 1606688.

Please do not adjust margins